ACS APPLIED MATERIALS & INTERFACES

Letter

Cite This: ACS Appl. Mater. Interfaces 2017, 9, 39895-39900

www.acsami.org

Electrical Homogeneity of Large-Area Chemical Vapor Deposited Multilayer Hexagonal Boron Nitride Sheets

Fei Hui,[‡,†,§] Wenjing Fang,[†,§] Wei Sun Leong,[§,⊥] Tewa Kpulun,[∥] Haozhe Wang,[§] Hui Ying Yang,[⊥] Marco A. Villena,[‡,#] Gary Harris,[∥] Jing Kong,[§] and Mario Lanza*[,‡]

[‡]Institute of Functional Nano & Soft Materials, Collaborative Innovation Center of Suzhou Nano Science and Technology, Soochow University, Suzhou 215123, China

[§]Department of Electrical Engineering and Computer Science, Massachusetts Institute of Technology, Cambridge, Massachusetts 02139, United States

[⊥]Pillar of Engineering Product Development, Singapore University of Technology and Design, 8 Somapah Road, Singapore 487372, Singapore

[∥]Department of Electrical and Computer Engineering, Howard University, Washington, D.C. 20059, United States

[#]Department of Materials Science and Engineering, Stanford University, Stanford, California 94305, United States

Supporting Information

ABSTRACT: Large-area hexagonal boron nitride (*h*-BN) can be grown on polycrystalline metallic substrates via chemical vapor deposition (CVD), but the impact of local inhomogeneities on the electrical properties of the *h*-BN and their effect in electronic devices is unknown. Conductive atomic force microscopy (CAFM) and probe station characterization show that the tunneling current across the *h*-BN stack fluctuates up to 3 orders of magnitude from one substrate (Pt) grain to another. Interestingly, the variability in the tunneling current across the *h*-BN within the same substrate grain is very low, which may enable the use of CVD-grown *h*-BN in ultra scaled technologies.

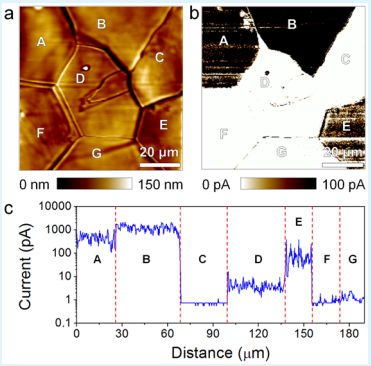

KEYWORDS: *hexagonal boron nitride, chemical vapor deposition, electrical homogeneity, conductive AFM, polycrystalline*

Hexagonal boron nitride (*h*-BN) is a layered insulator (direct band gap ~5.9 eV),[1] in which boron and nitrogen atoms arrange in a sp^2 hexagonal structure by covalent bonding, whereas the layers stick to each other by van der Waals attraction. Given its high in-plane mechanical strength (500 N/m),[2] large thermal conductivity (600 $Wm^{-1}K^{-1}$),[3] and high chemical stability (up to 1500 °C in air),[4] *h*-BN has attracted much attention for a wide range of potential applications. For example, thanks to their ultraflat surface free of dangling bonds, *h*-BN substrates can increase the mobility of graphene-based FETs up to ~140 000 cm^2V^{-1} s^{-1} [5] (on SiO_2 substrates it is lower, 15 000 cm^2 V^{-1} s^{-1}). But its use as dielectric in different types of devices (e.g., field effect transistors memristors) is much more promising, as *h*-BN has shown enhanced reliability (compared to HfO_2),[6] characteristic layer-by-layer dielectric breakdown process,[7] and resistive switching.[8,9]

Chemical vapor deposition (CVD) in ultra high vacuum (UHV),[10,11] atmospheric pressure (APCVD) and low pressure (LPCVD)[12−15] is an attractive approach to synthesize large-area *h*-BN stacks with low density of defects on metallic foils (e.g., Cu, Fe, Pt). Because of the high temperatures required for the CVD growth of *h*-BN (>800 °C), the metallic substrates become polycrystalline. ref.[15] reported that the thickness of the *h*-BN stack grown by CVD on polycrystalline Ni depends on the size of the Ni crystal underneath, and it was also suggested that *h*-BN grows faster on the surface of Ni (100) than Ni (111), because of the different catalytic reaction activities.[16] Similar observations have been recently reported for *h*-BN stacks grown via CVD on polycrystalline Pt substrates.[17] However, the impact of these thickness fluctuations on the local electrical properties of the *h*-BN stacks and their effect on the performance of electronic devices is still unknown. This information is essential to understand and control the device-to-device variability, which has been reported as one of the major problems of ultrascaled technologies.[18]

In this work, the electrical homogeneity of continuous, large-area and high-quality *h*-BN stacks (grown by LPCVD on Pt substrates) is investigated via conductive atomic force microscopy (CAFM) and probe station. We find that thicker *h*-BN preferably grows on Pt grains with (101) crystallographic

Received: July 1, 2017
Accepted: November 6, 2017
Published: November 7, 2017

DOI: 10.1021/acsami.7b09417
ACS Appl. Mater. Interfaces 2017, 9, 39895−39900

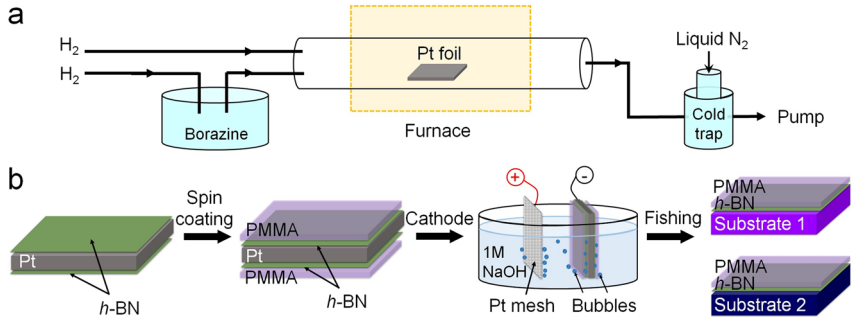

Figure 1. Hexagonal boron nitride growth and transfer. (a) Schematic of LPCVD process to grow *h*-BN on Pt foils. (b) Electrochemical (bubble) method to transfer *h*-BN from Pt foil to the target substrates.

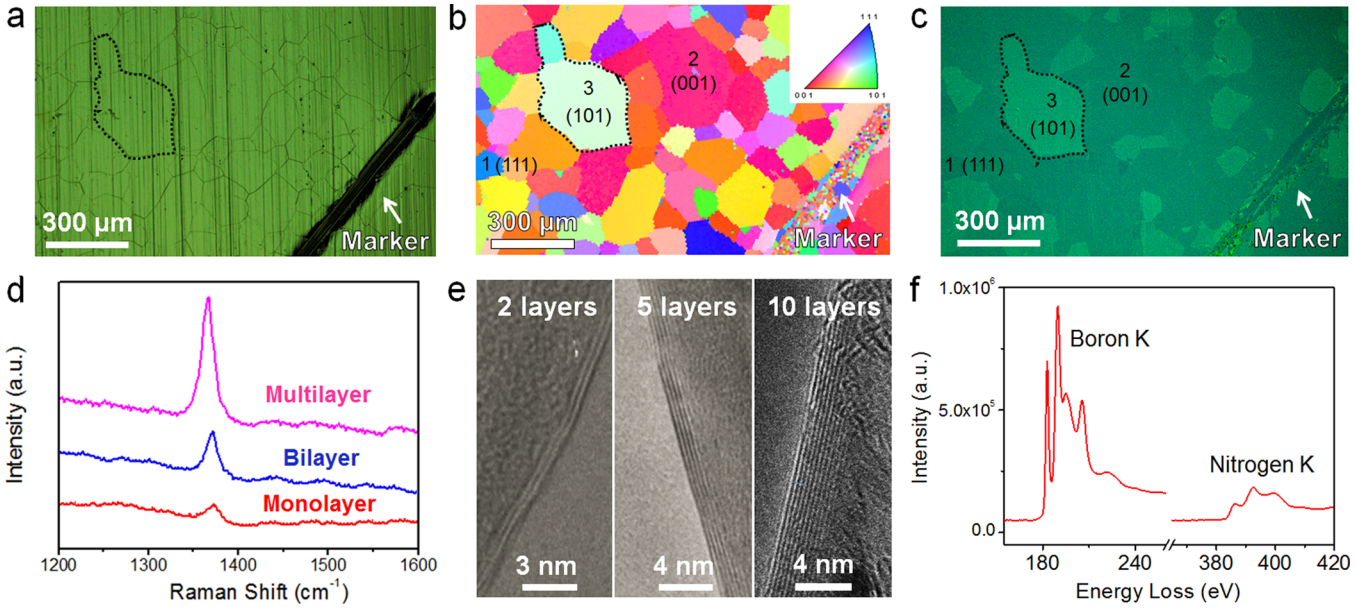

Figure 2. Characterization of *h*-BN films. (a) Optical microscope and (b) EBSD images of a polycrystalline Pt substrate before *h*-BN growth (annealed). The two images correspond to the same location of the sample, as highlighted by the marker in the right-bottom part. (c) Optical microscope image of a *h*-BN/300 nm-SiO_2/Si sample. The *h*-BN was grown on the area displayed in (a) and subsequently transferred onto a SiO_2/Si substrate. The granular pattern with different dark-green and light-green colors (thicknesses) observed in c perfectly matches the shape of the grains in (a). Therefore, it is possible to know which crystallographic orientation produces dark-green (thinner) and light-green (thicker) *h*-BN stacks. (d) Raman spectra collected on different locations of the *h*-BN/300 nm-SiO_2/Si sample. Monolayer/multilayer have been collected at dark-green/light-green locations of panel (c). (e) High-resolution TEM images demonstrating the different thicknesses and the good layered structure of the *h*-BN stacks. (f) EELS spectrum of *h*-BN showing the typical boron and nitrogen peaks.

orientation. The excellent topographic-current correlation observed in CAFM maps indicates that the tunneling current across the *h*-BN is homogeneous within each Pt grain, but very different from grain to grain. Device level tests revealed that the variability of the devices fabricated within the same Pt grain is very small, and that the properties of devices grown on different Pt grains are strongly different to each other. The results here presented provide new insights on the electrical homogeneity of large-area *h*-BN stacks, and contribute to understanding the variability of *h*-BN-based electronic devices.

Figure 1a shows the schematic of the LPCVD process for *h*-BN growth. A 1 cm × 2.5 cm Pt substrate was cleaned via thermal annealing (see the Supporting Information) and introduced in the center of the CVD tube (see Figure 1a). We use Pt as substrate because, despite being more expensive than Cu, Ni, or Fe, the quality of the *h*-BN grown on Pt is higher (i.e., it holds a better layer structure with less randomly oriented crystallities).[19] Liquid-phase borazine precursor was kept in a commercial cold container at 3 °C to avoid it is self-decomposition, and a cold trap filled with liquid nitrogen was used to prevent the damage of the pump. The borazine molecules (0.1 sccm) were delivered to the Pt substrate on H_2 carrier gas (70 sccm) at 950 °C, which produced their absorption and decomposition on the surface of the Pt substrate, and the self-mediated growth of *h*-BN. After the LPCVD growth, the *h*-BN stack was transferred onto 300 nm-SiO_2/Si for Raman spectroscopy and optical microscopy inspection, and on metallic grids for transmission electron microscopy (TEM) characterization. The transfer of the *h*-BN was carried out following the bubbling approach based on water electrolysis (see Figure 1b and Supporting Information).[19] This method is beneficial because it allows recycling the Pt foil for unlimited times (i.e., it is cost-effective).

Figure 2a and 2b show the optical image and electron backscatter diffraction (EBSD) map of a Pt substrate after the thermal annealing (before *h*-BN growth). Different Pt grains and crystallographic orientations can be distinguished. A long marker at the bottom right part of the image was made with a

DOI: 10.1021/acsami.7b09417
ACS Appl. Mater. Interfaces 2017, 9, 39895−39900

razor blade to identify this location in subsequent analyses. After that, multilayer *h*-BN was grown directly on the surface of the Pt substrate and transferred onto flat 300 nm-SiO_2/Si. The optical image of the *h*-BN/300 nm-SiO_2/Si (Figure 2c) reveals regions with different colors (dark-green to light-green) perfectly matching the shapes of the Pt grains before *h*-BN growth (Figures 2a and 2b). Figure 2c also proves that the *h*-BN stack is continuous, as well as the nondestructive nature of the bubbling transfer method. Interestingly, the *h*-BN stacks grown on Pt grains with crystallographic orientations near (101) show light-green colors in the optical microscope image (see Figure 2c), which has been attributed to a larger thickness.[15,17] This hypothesis has been verified by collecting Raman spectra at different locations on the surface of the *h*-BN/300 nm-SiO_2/Si sample (see Figure 2d). The dark-green grains in the optical microscope image (Figure 2c) always showed an E_{2g} peak near 1370 cm^{-1}, which corresponds to monolayer *h*-BN; on the contrary at the light-green grains the E_{2g} peak shifted toward ~1366 cm^{-1}, which is the characteristic value of bulk *h*-BN. High-magnification TEM images (Figure 2e) present the definitive corroboration of grain-dependent thickness in the *h*-BN stack. The thicknesses observed via TEM at multiple locations of the sample (Figure 2e) always ranged between 1 and 2 and 10−13 layers, meaning that the dark and light regions in Figure 2c should correspond to thicknesses of 1−2 and 10−13 layers, respectively. It is worth noting that, for all thicknesses, the TEM images reveal defect-free layered structure. The electron energy loss spectroscopy (EELS) spectrum (Figure 2f) shows two edges at around 180 and 390 eV, which correspond to the characteristic *k*-shell ionization edges of boron and nitrogen. This verifies that the stoichiometric ratio of boron and nitrogen is 1:1, which is characteristic of layered *h*-BN with hexagonal lattice.[2]

The electrical performance of as-grown *h*-BN/Pt (without transfer) has been tested via CAFM. Figures 3a, b show the simultaneously collected topographic and current maps (respectively) measured on the surface of the *h*-BN stack when applying a bias of −2 V to the Pt substrate (CAFM tip grounded). In order to analyze the electrical properties of *h*-BN grown on different Pt grains, we used a large (80 μm × 80 μm) scan size and strategically selected an area of the sample containing several Pt grains. The different Pt grains detected have been named with letters from A to G. Despite the *h*-BN cannot be detected in the topographic map (it is very flat compared to the Pt surface, see Figure S1), its effect can be clearly seen in the current map (Figure 3b), which reveals sharp conductivity changes from grain to grain. The different currents collected on each Pt grain must be related to the presence of *h*-BN stacks with different thicknesses because the underlying Pt grains, despite having different crystal orientations, hold similar conductivities.[20] It should be highlighted that the *h*-BN adhesion to the Pt surface is always by van der Waals forces for any Pt crystalline orientation, which means that the electronic coupling between the *h*-BN and Pt from one grain to another does not change. Therefore, *h*-BN/Pt electronic coupling is not one factor producing the conductivity changes from one grain to another observed in Figure 3b. The fact that the conductivity changes have been detected in the same image discards tip wearing from one grain to the other, and the perfect topography-current correlation undoubtedly demonstrate that *h*-BN grown on different grains hold different conductivities (because of their different thicknesses, as shown in Figure 2). It should be highlighted that, sporadically, the

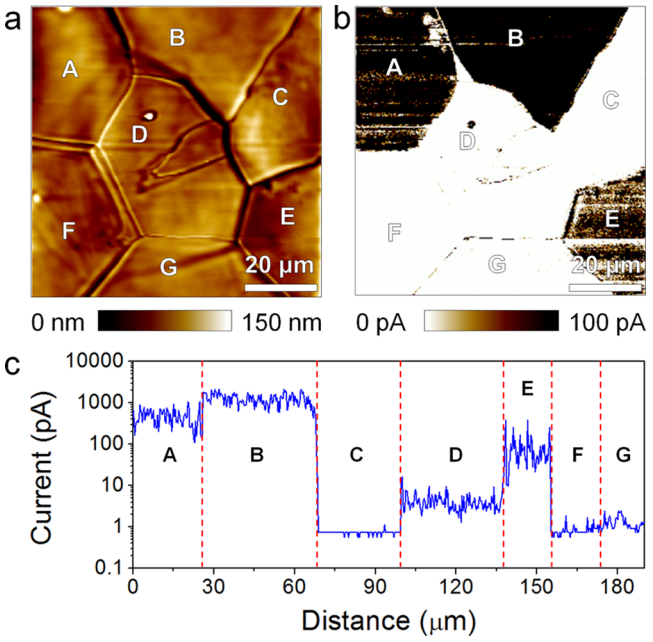

Figure 3. CAFM Characterization of as-grown *h*-BN/Pt. (a) Topographic and (b) current maps simultaneously collected on *h*-BN grown on a polycrystalline Pt substrate, under a bias of −2 V (applied to the substrate, tip grounded). (c) Assembly of cross-sections collected at the different grains of the current map in b.

regions close to the Pt grain boundaries have shown higher currents (see for example the grain boundaries between grains D-G and F-G). The explanation for this observation is as follows: when the metallic substrate is exposed to large temperatures it becomes polycrystalline; the grain boundaries of the metal substrate are rough and may contain asperities; these topographic accidents alter the *h*-BN growth, and at that location the *h*-BN may be thinner or even cracked, displaying large currents in the current maps. Cross sections have been collected (offline) at all the grains of the current image (Figure 3b) using the AFM software (NanoScope Analysis) and assembled one after the other (using OriginPro 8 software). The result is displayed in Figure 3c. Within each grain the current is homogeneous, and sharp changes are detected from grain to grain. As can be observed, the highest currents are detected on grain B, indicating that it holds the thinnest *h*-BN stack on its surface. Grain C shows negligible currents similar to the electrical noise of the CAFM, indicating that the −2 V applied were not enough to generate tunneling current across the *h*-BN stack. It should be emphasized that the current deviations within each grain are below 1 order of magnitude for all grains (compare maximum and minimum peaks within each grain in Figure 3c). This value is smaller than that observed in other thin insulating films (of similar thickness) being currently used in the industry, such as HfO_2 and TiO_2 (see Figure S3). Therefore, the electrical properties of *h*-BN within the same grain seem to be very homogeneous, which shows great potential to mitigate device-to-device variability problems of ultra scaled devices. Further electrical information about the grains has been obtained by measuring the onset voltage (V_{ON}) of the *h*-BN stacks on each Pt grain. The onset voltage is defined as the minimum voltage that needs to be applied between the CAFM tip and the substrate of the sample (Pt) in order to observe tunneling currents above the noise level.[21] Despite the noise level of our CAFM being ~1 pA, we selected

DOI: 10.1021/acsami.7b09417
ACS Appl. Mater. Interfaces 2017, 9, 39895−39900

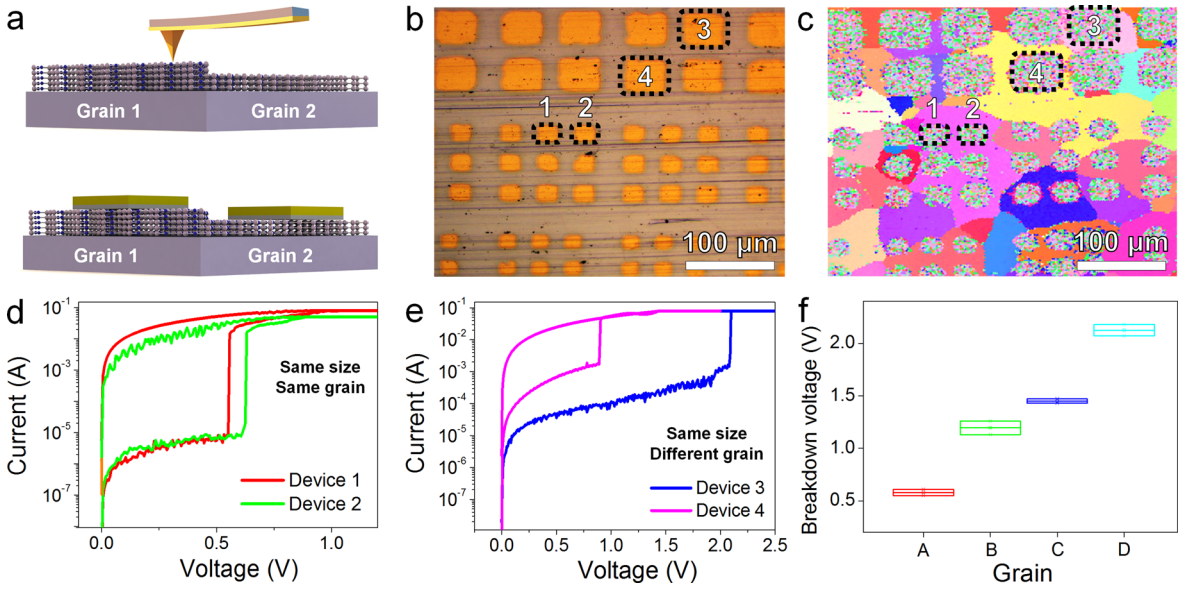

Figure 4. Device level characterization of *h*-BN stacks. (a) Schematic of as-grown *h*-BN/Pt (top) and *h*-BN-based devices (bottom). The device cell is an Au/Ti/*h*-BN/Pt structure. (b) Optical image and (c) EBSD map of matrixes of Au/Ti/*h*-BN/Pt cells with different lateral sizes. As this map has been collected with the presence of *h*-BN, it is only meaningful to distinguish different grains, not to assess the real crystallographic orientation of each grain. For this reason, the color scale has been intentionally removed. (d) *I*−*V* curves collected on two devices with the same size (25 μm × 25 μm) within the same Pt grain. (e) *I*−*V* curves collected on two devices with the same size (50 μm × 50 μm) located at different Pt grains. (f) Analysis of the BD voltage for Au/Ti/*h*-BN/Pt devices patterned on 4 different Pt grains (located outside the region of c).

V_{ON} = *V* (*I* = 5 pA) in order to be completely sure that non-negligible current is flowing across the *h*-BN stack. For this experiment, V_{ON} has been extracted by measuring individual current maps on each grain (1 μm × 1 μm). The results obtained (Table S1), strongly support the observations in Figure 3: the smallest V_{ON} (0.1 V) was detected on grain B, and the highest (6 V) on grain C. By fitting current vs voltage (I−*V*) curves collected on the *h*-BN at different Pt grains to the tunneling model equations it can be concluded that the real thickness of the *h*-BN stack fluctuates between 1 and 13 layers (see modeling section in the Supporting Information), in agreement with Figure 2e.

Finally, the electrical properties of *h*-BN stacks grown on polycrystalline Pt substrates have been analyzed at the device level using matrixes of metal/insulator/metal (MIM) cells (i.e., Au/Ti/*h*-BN/Pt). Figure 4a shows the schematic of as-grown *h*-BN on polycrystalline Pt foil before and after electrodes deposition, in which *h*-BN film serves as insulating layer between the top (Au/Ti) and bottom (Pt) metal electrodes. The optical microscope image of the sample after Au/Ti electrode deposition is shown in Figure 4b. The corresponding EBSD map of the same area of the sample has been also collected (Figure 4c). It should be highlighted that, unlike in Figure 2b, in Figure 4c the EBSD map has been collected in the presence of *h*-BN on the Pt substrate. As the *h*-BN is an insulator, this may distort the signal related to the local crystallographic orientation. For this reason, the EBSD map in Figure 4d will be only used to distinguish different grains (in that case the contrast is large) but not to identify which is the real crystallographic orientation of the Pt within each grain. For this reason, the color scale in Figure 4c has been intentionally removed. Several devices on the same and different Pt grains have been tested in the probe station by applying ramped voltage stresses (RVS), and the resulting current vs voltage (*I*−*V*) curves have been compared. As an example, Figure 4d shows the *I*−*V* curves collected on two devices with the same size (25 μm × 25 μm) that belong to the same Pt grain (devices 1 and 2 in Figure 4c). As it can be observed, the *I*−*V* characteristics for devices 1 and 2 are strikingly similar: *i)* the BD voltages (V_{BD}) show very small deviation (0.55 V and 0.61 V); (ii) the pre- and post-BD currents ($I_{PRE\text{-}BD}$ and $I_{POST\text{-}BD}$, respectively) almost overlap, and (iii) the $I_{POST\text{-}BD}/I_{PRE\text{-}BD}$ ratio is identical. These results are indeed indicating that the device-to-device variability within the same Pt grain is very small. Any potential variability of the prebreakdown *I*−*V* curves in devices within the same Pt grain should be related to nanoscale inhomogeneities within the *h*-BN stack, such as thickness fluctuations (see Figure S2), local defects, *h*-BN domain boundaries, and/or wrinkles. Nevertheless, as displayed in Figures 4d and 3c and Figure S3 the variability of the electrical properties of the *h*-BN within the same Pt grain are very small. On the contrary, the devices with the same size but patterned on different Pt grains show very inhomogeneous *I*−*V* characteristics. As an example, Figure 4e shows the *I*−*V* curves collected on devices 3 and 4 (see Figure 4c). First, the pre-BD currents are very different; second, V_{BD} for both devices are remarkably different: 2.09 V for device 3 and 0.89 V for device 4; and third, the $I_{POST\text{-}BD}/I_{PRE\text{-}BD}$ ratio is also slightly different. The different electrical properties of devices 3 and 4 are related to the different thicknesses of the *h*-BN stack, due to the different crystallographic orientation of the underlying Pt grain. These observations have been corroborated by measuring additional MIM devices at different Pt grains. As Figure 4f shows, the deviation of V_{BD} within each grain is very small (from ±0.013 V for grain C to ±0.054 V for grain B), but the deviations of V_{BD} from one Pt grain to another are large (from 0.58 V in grain A to 2.13 V in grain D). The breakdown event observed for all devices (displayed as a sharp current increase in Figure 4d, e) further demonstrates that the *h*-BN sheet grown on the Pt substrate is continuous, otherwise a larger current under smaller voltage (i.e., 1×10^{-2} A @ 0.1 V) typical of shorted devices should be observed.

DOI: 10.1021/acsami.7b09417
ACS Appl. Mater. Interfaces 2017, 9, 39895−39900

Fortunately, cutting-edge electronic devices based on MIM cells cover ultra scaled areas. In the case of FETs, the current technology node is 7 nm, and the total length of current FETs never exceeds 50 nm. In the case of memristors and other nonvolatile memories, such as resistive random access memories (RRAM), phase change random access memories (PCRAM) and ferroelectric random access memories (FeRAM), device areas down to 10 nm × 10 nm are preferred.[22] Therefore, as the diameter of the Pt grains easily surpass 100 μm, the fabrication of *h*-BN based electronic devices with very low variability is feasible. More efforts toward the growth of large-area single-crystalline *h*-BN stacks should conduct to ultralow variability technologies.

In conclusion, the electrical homogeneity of *h*-BN stacks grown via CVD on Pt substrates has been analyzed by CAFM and a probe station. We observe that *h*-BN grows thicker on Pt grains with crystallographic orientations close to (101). In situ CAFM characterization reveals that the tunneling current across the *h*-BN grown on the same Pt grain is very homogeneous (i.e., more homogeneous than that observed in other insulators being currently used in the industry, such as HfO_2 and TiO_2), but sharp conductivity changes are detected from grain to grain. Device level tests in the probestation reveal that the variability of Au/Ti/*h*-BN/Pt devices within each grain is strikingly low in terms of $I_{PRE\text{-}BD}$, $I_{POST\text{-}BD}$, and V_{BD}. These results contribute to the understanding of the electrical properties of *h*-BN and variability of *h*-BN-based electronic devices.

■ ASSOCIATED CONTENT

Supporting Information

The Supporting Information is available free of charge on the ACS Publications website at DOI: 10.1021/acsami.7b09417.

Additional experimental explanations, AFM characterization of the *h*-BN/300 nm-SiO_2/Si sample, electrical measurements, and modeling details (PDF)

■ AUTHOR INFORMATION

Corresponding Author

*E-mail: mlanza@suda.edu.cn.

ORCID

Wei Sun Leong: 0000-0001-8131-2468
Hui Ying Yang: 0000-0002-2244-8231
Mario Lanza: 0000-0003-4756-8632

Author Contributions

†F.H. and W.F. contributed equally to this work. The manuscript was written through contributions of all authors. All authors have given approval to the final version of the manuscript.

Notes

The authors declare no competing financial interest.

■ ACKNOWLEDGMENTS

F.H. acknowledges the support from the Young 1000 Global Talent Recruitment Program of the Ministry of Education of China, the National Natural Science Foundation of China (Grants 61502326, 41550110223, 11661131002), the Jiangsu Government (Grant BK20150343), the Ministry of Finance of China (Grant SX21400213) and the Young 973 National Program of the Chinese Ministry of Science and Technology (Grant 2015CB932700). The Collaborative Innovation Center of Suzhou Nano Science & Technology, the Jiangsu Key Laboratory for Carbon-Based Functional Materials & Devices, the Priority Academic Program Development of Jiangsu Higher Education Institutions, and the Opening Project of Key Laboratory of Microelectronic Devices & Integrated Technology (Institute of Microelectronics, Chinese Academy of Sciences) are also acknowledged. W.F., T.K., G.H., and J.K. acknowledge the support from the STC Center for Integrated Quantum Materials, NSF Grant DMR-1231319. H.W. and J.K. acknowledge the support from NSF DMR/ECCS−1509197. W.S.L. acknowledges the support from SUTD-MIT Postdoctoral Fellows Program.

■ REFERENCES

(1) Watanabe, K.; Taniguchi, T.; Kanda, H. Direct-bandgap Properties and Evidence for Ultraviolet Lasing of Hexagonal Boron Nitride Single Crystal. *Nat. Mater.* **2004**, *3*, 404−409.

(2) Song, L.; Ci, L. J.; Lu, H.; Sorokin, P. B.; Jin, C. H.; Ni, J.; Kvashnin, A. G.; Kvashnin, D. G.; Lou, J.; Yakobson, B. I.; Ajayan, P. M. Large Scale Growth and Characterization of Atomic Hexagonal Boron Nitride Layers. *Nano Lett.* **2010**, *10*, 3209−3215.

(3) Lindsay, L.; Broido, D. A. Enhanced Thermal Conductivity and Isotope Effect in Single-Layer Hexagonal Boron Nitride. *Phys. Rev. B: Condens. Matter Mater. Phys.* **2011**, *84*, 155421.

(4) Liu, Z.; Gong, Y. J.; Zhou, W.; Ma, L. L.; Yu, J. J.; Idrobo, J. C.; Jung, J.; MacDonald, A. H.; Vajtai, R.; Lou, J.; Ajayan, P. M. Ultrathin High-Temperature Oxidation-Resistant Coatings of Hexagonal Boron Nitride. *Nat. Commun.* **2013**, *4*, 2541.

(5) Dean, C. R.; Young, A. F.; Meric, I.; Lee, C.; Wang, L.; Sorgenfrei, S.; Watanabe, K.; Taniguchi, T.; Kim, P.; Shepard, K. L.; Hone, J. Boron Nitride Substrates for High-Quality Graphene Electronics. *Nat. Nanotechnol.* **2010**, *5*, 722−726.

(6) Ji, Y. F.; Pan, C. B.; Zhang, M. Y.; Long, S. B.; Lian, X. J.; Miao, F.; Hui, F.; Shi, Y. Y.; Larcher, L.; Wu, E.; Lanza, M. Boron Nitride as Two Dimensional Dielectric: Reliability and Dielectric Breakdown. *Appl. Phys. Lett.* **2016**, *108*, 012905.

(7) Hui, F.; Pan, C. B.; Shi, Y. Y.; Ji, Y. F.; Grustan-Gutierrez, E.; Lanza, M. On the Use of Two Dimensional Hexagonal Boron Nitride as Dielectric. *Microelectron. Eng.* **2016**, *163*, 119−133.

(8) Pan, C. B.; Ji, Y. F.; Xiao, N.; Hui, F.; Tang, K. C.; Guo, Y. Z.; Xie, X. M.; Puglisi, F. M.; Larcher, L.; Miranda, E.; Jiang, L. L.; Shi, Y. Y.; Valov, I.; McIntyre, P. C.; Waser, R.; Lanza, M. Coexistence of Grain-Boundaries-Assisted Bipolar and Threshold Resistive Switching in Multilayer Hexagonal Boron Nitride. *Adv. Funct. Mater.* **2017**, *27*, 1604811.

(9) Hui, F.; Grustan-Gutierrez, E.; Long, S.; Liu, Q.; Ott, A. K.; Ferrari, A. C.; Lanza, M. Graphene and Related Materials for Resistive Random Access Memories. *Adv. Electron. Mater.* **2017**, *3*, 1600195.

(10) Nagashima, A.; Tejima, N.; Gamou, Y.; Kawai, T.; Oshima, C. Electronic States of Monolayer Hexagonal Boron Nitride Formed on the Metal Surfaces. *Surf. Sci.* **1996**, *357*, 307−311.

(11) Nagashima, A.; Tejima, N.; Gamou, Y.; Kawai, T.; Oshima, C. Electronic Dispersion Relations of Monolayer Hexagonal Boron Nitride Formed on the Ni(111) Surface. *Phys. Rev. B: Condens. Matter Mater. Phys.* **1995**, *51*, 4606−4613.

(12) Kim, S. M.; Hsu, A.; Park, M. H.; Chae, S. H.; Yun, S. J.; Lee, J. S.; Cho, D. H.; Fang, W. J.; Lee, C. G.; Palacios, T.; Dresselhaus, M.; Kim, K. K.; Lee, Y. H.; Kong, J. Synthesis of Large-Area Multilayer Hexagonal Boron Nitride for High Material Performance. *Nat. Commun.* **2015**, *6*, 8662.

(13) Kim, K. K.; Hsu, A.; Jia, X. T.; Kim, S. M.; Shi, Y. M.; Hofmann, M.; Nezich, D.; Rodriguez-Nieva, J. F.; Dresselhaus, M.; Palacios, T.; Kong, J. Synthesis of monolayer hexagonal boron nitride on Cu foil using chemical vapor deposition. *Nano Lett.* **2012**, *12*, 161−166.

(14) Gao, Y.; Ren, W. C.; Ma, T.; Liu, Z. B.; Zhang, Y.; Liu, W. B.; Ma, L. P.; Ma, X. L.; Cheng, H. M. Repeated and controlled growth of monolayer, bilayer and few-layer hexagonal boron nitride on Pt foil. *ACS Nano* **2013**, *7*, 5199.

DOI: 10.1021/acsami.7b09417
ACS Appl. Mater. Interfaces 2017, 9, 39895−39900

(15) Shi, Y. M.; Hamsen, C.; Jia, X. T.; Kim, K. K.; Reina, A.; Hofmann, M.; Hsu, A. L.; Zhang, K.; Li, H.; Juang, Z. Y.; Dresselhaus, M. S.; Li, L. J.; Kong, J. Synthesis of Few-Layer Hexagonal Boron Nitride Thin Film by Chemical Vapor Deposition. *Nano Lett.* **2010**, *10*, 4134−4139.
(16) Lee, Y. H.; Liu, K. K.; Lu, A. Y.; Wu, C. Y.; Lin, C. T.; Zhang, W. J.; Su, C. Y.; Hsu, C. L.; Lin, T. W.; Wei, K. H.; Shi, Y. M.; Li, L. J. Growth Selectivity of Hexagonal-Boron Nitride Layers on Ni with Various Crystal Orientations. *RSC Adv.* **2012**, *2*, 111−115.
(17) Park, J. H.; Park, J. C.; Yun, S. J.; Kim, H.; Luong, D. H.; Kim, S. M.; Choi, S. H.; Yang, W.; Kong, J.; Kim, K. K.; Lee, Y. H. Large-Area Monolayer Hexagonal Boron Nitride on Pt Foil. *ACS Nano* **2014**, *8*, 8520−8528.
(18) Allan, A. *International Technology Roadmap for Semiconductors of 2008*. https://cseweb.ucsd.edu/classes/wi09/cse242a/itrs/ORTC.pdf, accessed February, 2016.
(19) Kim, G.; Jang, A. R.; Jeong, H. Y.; Lee, Z.; Kang, D. J.; Shin, H. S. Growth of High-Crystalline, Single-Layer Hexagonal Boron Nitride on Recyclable Platinum Foil. *Nano Lett.* **2013**, *13*, 1834−1839.
(20) Powell, R. W.; Tye, R. P.; Woodman, M. J. The Thermal Conductivity and Electrical Resistivity of Polycrystalline Metals of the Platinum Group and of Single Crystals of Ruthenium. *J. Less-Common Met.* **1967**, *12*, 1−10.
(21) Lanza, M.; Porti, M.; Nafría, M.; Aymerich, X.; Ghidini, G.; Sebastiani, A. Trapped Charge and Stress Induced Leakage Current (SILC) in Tunnel SiO2 Layers of De-processed MOS Non-Volatile Memory Devices Observed at the Nanoscale. *Microelectron. Reliab.* **2009**, *49*, 1188−1191.
(22) Govoreanu, B.; Kar, G. S.; Chen, Y. Y.; Paraschiv, V.; Fantini, A.; Radu, I. P.; Goux, L.; Clima, S.; Degraeve, R.; Jossart, N. 10 × 10nm2 Hf/HfOx Crossbar Resistive RAM with Excellent Performance, Reliability and Low-Energy Operation. *IEEE Int. Electron Dev. Meeting* **2011**, *11*, 729−732.

DOI: 10.1021/acsami.7b09417
ACS Appl. Mater. Interfaces 2017, 9, 39895−39900